Solar Energy Materials & Solar Cells 128 (2014) 386–393

Contents lists available at ScienceDirect

Solar Energy Materials & Solar Cells

journal homepage: www.elsevier.com/locate/solmat

Synergistic effect of surface plasmonic particles in PbS/TiO_2 heterojunction solar cells

Bo Ding [a], Tongchuan Gao [b], Yang Wang [c], David H. Waldeck [c], Paul W. Leu [b], Jung-Kun Lee [a,*]

[a] Department of Mechanical Engineering & Material Science, University of Pittsburgh, Pittsburgh, PA 15261, USA
[b] Department of Industrial Engineering, University of Pittsburgh, Pittsburgh, PA 15261, USA
[c] Department of Chemistry, University of Pittsburgh, Pittsburgh, PA 15260, USA

ARTICLE INFO

Article history:
Received 8 February 2014
Received in revised form
20 May 2014
Accepted 1 June 2014
Available online 25 June 2014

Keywords:
Surface plasmons
Core–shell particles
Thin film solar cells
PbS

ABSTRACT

Core–shell particles composed of a dielectric core and a metallic nanoshell exhibit tunable surface plasmons that may be exploited to enhance the light absorption capability of photoactive materials. This work uses both experimental and theoretical methods to elucidate the mechanism by which SiO_2@Au@SiO_2 (SGS) core–shell–shell particles improve the light harvesting efficiency of PbS–TiO_2 heterojunction solar cells. The enhanced light absorption by PbS nanoparticles depends on their location in the device and their impact on device morphology. This study demonstrates that SGSs can promote the light harvesting of thin film solar cells in two ways. First, the localized surface plasmon resonance of the SGSs increases light scattering and the local electromagnetic field at the PbS–SGS interface. Second, placing SGSs between the PbS and TiO_2 layers, forms nanodomes on top Au electrode and gives rise to additional light scattering that enhances the light harvesting efficiency. By combining these effects the short circuit current density and the energy conversion efficiency are increased by 29% and 24% respectively compared to a cell without SGSs.

1. Introduction

Lead chalcogenide semiconductors have attracted scientific and technological interest because of their large optical cross section, tunable bandgap, and low-cost solution processability [1]. In particular, quantum dots (QDs) of *p*-type lead chalcogenide are excellent light absorbers in the visible and near IR region, which is advantageous in solar cells [2]. If the photon energy is larger than the bandgap of lead chalcogenide by two times or more, the excess energy of the hot carrier produced in QDs can be converted to multiple excitons via an inverse Auger type process and the incident photon-to-electron conversion efficiency (IPCE) can exceed 100% [3]. Hence, lead chalcogenide QDs have been considered as a promising light absorber for high efficiency solar cells [4–6], and different types of solar cells using such QDs have been proposed. Recently, a layer of wide bandgap semiconductor such as ZnO [7,8] or TiO_2 [9,10] has been inserted between the QD film and a transparent conducting oxide (TCO) film to form a depletion region where the built-in potential enhances exciton dissociation and directional electron flow. In planar heterojunction QD solar cells, the tradeoff between light absorption and carrier extraction is an important issue [11,12]. As the thickness of the QD film increases to several hundred nanometers, it can absorb more incoming photons, which increases the light collection efficiency. However if the minority carrier diffusion length becomes comparable to the QD film thickness, then the carrier recombination probability increases and the charge collection efficiency of the solar cells decreases [5]. Thus, a need exists to increase the light absorption without changing the QD layer thickness in heterojunction QD solar cells.

Surface plasmons have been extensively studied for the past decade, in part because they can improve the light harvesting efficiency of solar cells. Metallic nanostructures can increase both the near-field intensity and the light scattering efficiency of a device [13]. If a light absorbing semiconductor is located near a plasmonic structure, the increase in the local field intensity can enhance the semiconductor's light absorption. Therefore, plasmonic nanostructures have been employed in traditional silicon based solar cells [14–16] and in emerging types of solar cells, such as dye sensitized solar cells and organic solar cells, to improve their light harvesting efficiency [17–21]. It is important to match the surface plasmon frequency with the light absorption spectrum of the photoactive materials. Different metallic nanostructures have been studied such as nanoshells [22–24], nanocages [25,26], nanoeggs [27–29] and

* Corresponding author.
E-mail address: jul37@pitt.edu (J.-K. Lee).

http://dx.doi.org/10.1016/j.solmat.2014.06.001
0927-0248/

nanorods [30–32] where various morphologies provide a way to tune the localized surface plasmon resonance (LSPR) and optimize the light harvesting efficiency of the photovoltaic (PV) devices [33,34]. In particular, plasmonic core–shell nanostructures, consisting of a silica sphere as the dielectric core and a metal as the nanoshell, have been successfully utilized in PV devices such as dye sensitized solar cells and QD solar cells [35–38].

This work reports on the use of plasmonic SiO_2@Au@SiO_2 (SGS) core–shell–shell particles (a schematic of the SGS particle is shown in Fig. 1b) to enhance the photon–electron conversion efficiency in PbS QD solar cells. The outer silica layer, which overcoats the intermediate Au shell, is expected to enhance its chemical stability and inhibit carrier trapping by the metal shell. This study examines the effect of the location of SGS particles on the performance of PbS QD solar cells. Two different designs for the SGS placement are considered, namely at the PbS–Au interface or the PbS–TiO_2 interface. The results show that placing the SGSs at the PbS–TiO_2 interface enhances the energy conversion efficiency of PbS solar cells through two different mechanisms: an increase of the local electromagnetic field intensity associated with the LSPR of the SGSs and additional light scattering by nanodome structures that are formed on top of Au electrode.

2. Methods

2.1. Materials

Tetra-ethoxysilane (TEOS, 98%), ammonium hydroxide (28–30%), (3-aminopropyl)trimethoxysilane (APTMS, 97%), tetrachloroauric

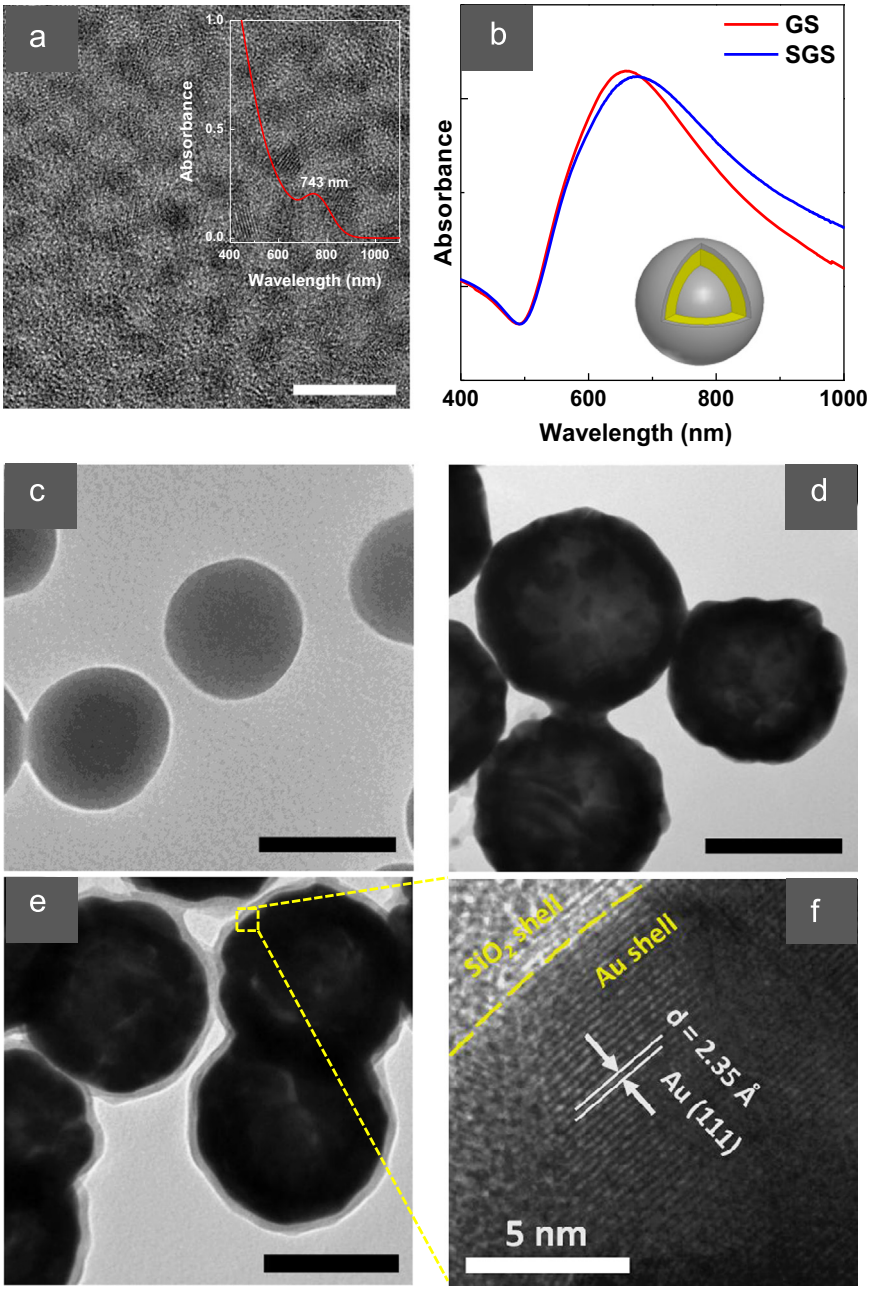

Fig. 1. (a) HRTEM images are shown for PbS QDs with a diameter of 3.0 ± 0.4 nm (a scale bar is 10 nm). (b) Absorbance spectra are shown for GSs and SGSs dispersed in deionized water (an inset is a schematic of the silica core–gold shell–silica shell particle). Panels (c–e) show the morphology evolution of the SGS particles through their preparation (a scale bar is 100 nm): (c) bare silica spheres with a diameter of ~90 nm, (d) Au@SiO_2 core–shell particles with a 20 nm thick Au shell, (e) SGSs with another outer silica shell of ~7 nm thickness, and (f) HRTEM image of the Au nanoshell.

acid ($HAuCl_4 \cdot 3H_2O$), tetrakis-hydroxymethylphosphonium chloride (THPC), sodium hydroxide (NaOH), potassium carbonate (K_2CO_3), polyvinylpyridine (PVP, MW=40,000), lead oxide (PbO), oleic acid (OA), octadecene (ODE), hexamethyldisilathiane (TMS), 1,2-ethanedithiol (EDT), hexane (anhydrous), and acetonitrile (anhydrous) were all purchased from Aldrich and used as received. Ethanol (200 proof, anhydrous) was bought from Decon Laboratories Inc. and formaldehyde (36.5–38%) from EMD Millipore and methanol (99.8%) from J.T. Baker. Ultrapure water (18.2 MΩ resistivity) was deionized using Milli-Q purification system (Millipore, MA).

2.2. Synthesis of SiO_2@Au@SiO_2 core–shell–shell spheres (SGSs)

The SGSs were synthesized following a procedure similar to those reported in the literature [45,46,50]. Initial uniform SiO_2 spheres with an average diameter of 90 nm were prepared via the Stöber method [51]. A mixture of 50 ml silica/ethanol solution (c=1 g/L) and 20 μL of APTMS was stirred vigorously at room temperature for 12 h and then refluxed at 78 °C for 1 h, in order to functionalize the surface of the silica spheres with APTMS molecules. The functionalized silica spheres were centrifuged and redispersed in pure ethanol several times to remove the excess APTMS. An aqueous solution (50 ml, $c \approx 9.9 \times 10^{-6}$ mol/L) of gold nanoparticles with a diameter of ~2 nm were prepared via Duff's method [52], and further diluted to 100 ml. The as-formed silica/ethanol solution was concentrated to 25 ml, and added drop-by-drop to this rapidly stirred aqueous Au NP solution. After stirring for 12 h at room temperature, non-attached gold nanoparticles were removed by centrifugation, leaving behind silica spheres decorated with gold nanoparticles through the gold–amine interactions. The attached gold seeds act as nucleation sites for further gold shell growth. An Au plating solution was prepared by adding 17.1 mg (25 mM) $HAuCl_4 \cdot 3H_2O$ and 124.5 mg (1.8 mM) of K_2CO_3 into 100 ml deionized water. The seeded silica aqueous solution was aged for 2 days and added dropwise to this solution as it was vigorously stirred at room temperature. The $AuCl^-$ ions' reduction started after 200 μL of formaldehyde was added to the mixture, and a complete gold nanoshell with a thickness of 25 nm was formed within 20 min. In order to overcoat another silica shell on the Au@SiO_2 particles (GSs), 10 ml of 0.5 mM PVP aqueous solution was immediately added to the pristine GSs aqueous solution. After stirring for another 24 h, the PVP stabilized GSs were centrifuged and purified in deionized water and ethanol several times. The resulting particles were redispersed in 194 ml of pure ethanol, with a subsequent addition of 8.5 ml of ammonium hydroxide and 0.9 ml of TEOS solution (10 vol% in pure ethanol). This mixture was then stirred for 12 h at room temperature to form SGSs. The final product was washed by pure ethanol and redispersed in methanol.

2.3. Synthesis of PbS colloidal quantum dots

PbS QDs with an excitonic peak at 740 nm were prepared via a procedure that Hines and Scholes reported [53]. All the reactions were carried out using a standard Schlenk line system. Typically, the lead oleate precursor was formed by heating and vigorously stirring the mixture, which contained 90 mg of PbO, 0.25 ml of OA and 3.75 ml of ODE, in a 50 ml three-necked flask at 150 °C for 30 min under an Ar gas atmosphere. After this precursor solution was cooled to 120 °C, 42 μL of TMS in 2 ml of ODE was swiftly injected into it with a sudden drop of the reaction temperature to 100 °C. The reaction temperature was kept at 100 °C for 30 s, and then the heat was removed to let the solution cool down to room temperature. PbS QDs were purified by repeated precipitation with acetone and dispersion with toluene, and finally dispersed in hexane.

2.4. Device fabrication

Patterned fluorine-doped tin oxide (FTO) (Pilington TEC 8) coated glass substrates were cleaned by immersing them in an ethanol/acetone (1:1) mixture under sonication for 10 min. The TiO_2 sol made of titanium tetraisopropoxide (TTIP) acidic solution was spin coated on the precleaned FTO and subsequently annealed in O_2 at 500 °C for 2 h, resulting in an 80 nm hole blocking layer. Next the TiO_2 nanoparticles were prepared using a hydrothermal method. And then a small amount of ammonium hydroxide was added into the TiO_2 slurry to increase its viscosity and form a TiO_2 paste. The paste was printed on a blocking layer coated FTO substrate by a doctor-blade method [35,36]. After annealing at 450 °C for 30 min under an N_2 gas atmosphere, a second TiO_2 film with a thickness of ~1 μm was formed. In order to build a planar heterojunction for carrier separation on top of this TiO_2 mesoporous film, a PbS QD film was prepared by a layer-by-layer dip coating method in an Ar gas filled glove box. Typically, the substrate with the TiO_2 film was immersed into a PbS QDs/hexane solution (20 mg/ml) by hand, and after 5 s it was slowly dragged out of the solution at a velocity of ~0.2 cm s^{-1}. Subsequently, the film was dipped into 0.1 M EDT/acetonitrile for 10 s and quickly removed. This dipping procedure was repeated fourteen times, resulting in a 150 nm thick, and densely packed, PbS film.

In order to locate a monolayer of the SGSs on top of the PbS film (or inside of the film), a diluted SGSs/methanol solution was drop-coated on the sample after (or before) the PbS QDs deposition. Loosely attached SGS particles were washed away by methanol after solvent was evaporated. SGSs coverage is ~20% of the substrate area. Similarly, SiO_2 spheres with a diameter of 150 nm were prepared by the Stöber method and a diluted SiO_2/methanol solution was drop-coated on the TiO_2 film as a control sample. Finally, the 20 nm-thick gold layer was deposited onto the PbS film by electron beam evaporation. The active area of the solar cells was 0.04 cm^2.

2.5. GSs, SGSs and PbS QDs characterization

Morphologies of GSs, SGSs and PbS QDs were examined by high-resolution electron microscopy (HRTEM, JEOL JEM-2100F) and scanning electron microscopy (SEM, Philips XL 30). Energy dispersive X-ray spectroscopy attached to electron microscopes was used to analyze the composition of films. The optical properties of the SGSs and multilayer films were measured by a UV–vis spectrophotometer (Lambda 35, Perkin Elmer).

2.6. Device characterization

J–V curves were measured under AM 1.5G simulated sunlight (PV Measurements, Inc.) with the aid of the electrochemical workstation (CH Instruments, CHI 660C). The electrochemical impedance spectroscopy (EIS) measurement was performed over a frequency range from 0.1 Hz to 1 kHz with the maximum electric potential of 0.05 V, and the external bias with a magnitude of open circuit voltage was applied. Incident photon to current efficiency curves (IPCE) of the solar cell was measured by illuminating the sample with a monochromatic beam over the wavelength range from 350 nm to 1100 nm (Model 74100, Newport Corp.). The electron lifetime was checked by an open-circuit voltage decay (OCVD) technique [54], in which the light source was a laser diode (λ=660 nm) driven by a function generator (Agilent 33220A) to provide square wave modulated illumination, and the changes in the photovoltage was monitored by a digital oscilloscope (Tektronix, TDS2024B).

2.7. Simulation

Numerical simulations were carried out using a finite-difference time-domain (FDTD) method to solve Maxwell's equations. A commercial package that was developed by Lumerical Solutions, was used for the electrodynamic simulation. The top boundary in the simulation super cell consists of perfectly matched layer and the sides consist of symmetric and anti-symmetric boundary conditions to model the periodic nature of the SGSs.

3. Results and discussions

The open circuit voltage of QD solar cells depends on the Fermi level difference across the *p*–*n* junction, and it can be tuned by changing the particle size of the PbS QDs [9]. This study uses PbS QDs with a diameter of 3.0 ± 0.3 nm and a first excitonic peak at ~740 nm or 1.67 eV (Fig. 1a). The average diameter of the PbS QDs was determined from transmission electron microscope (TEM) images. The PbS QD film was deposited using a layer-by-layer dip coating method [39]. During the deposition process, a long oleate capping chain on the QDs was exchanged with a short thiol ligand 1,2-ethanedithiol (EDT), in order to reduce the distance between adjacent QDs and increase the electric conductivity of the PbS film.

By changing the radius of the inner core and the shell thickness, the SGS localized surface plasmon resonance (LSPR) frequency can be tuned [23]. Based on a rough survey of sizes, SGSs that consist of a 90 nm diameter silica core, a 20 nm gold intermediate layer, and a 7 nm outer silica shell were chosen as the plasmonic scatterers, because they exhibit increased light absorption and scattering from 600 nm to 1000 nm where the PbS QDs bandgap (1.67 eV) lies [40–43]. SGS spheres were prepared by a two-step metallization process of the silica spheres [44,45]. First Au seeds (~2 nm in diameter) were decorated on the surface of (3-aminopropyl) trimethoxysilane (APTMS) functionalized silica cores, and then Au was reduced from a $AuCl^-$ ion solution onto the seeded surface to form a complete Au shell on the silica sphere. Subsequently, a continuous silica passivation shell was formed on top of the Au shell [46]. The outer silica shell was kept thinner than 10 nm in order to minimize changes in the near-field intensity at the outer silica shell [47].

Low resolution scanning electron microscope (SEM) images and electron dispersive spectroscopy (EDS) element analysis of the GSs and SGSs are shown in Fig. S1. The optical absorbance spectra (Fig. 1b) of the GSs and SGSs were measured, and the main plasmon peaks are located at 660 nm and 680 nm, respectively. The red-shift of the plasmon peak from the GS to the SGS is caused by the change in the effective dielectric constant that arises from the outer silica shell. The transmission electron microscopy (TEM) images in Fig. 1c–e show how the morphology evolves from bare silica spheres (~90 nm in diameter, panel c), to the Au@SiO_2 particles (panel d), and finally, to the SGS particles (panel e). The high resolution TEM (HRTEM) image in Fig. 1f shows that the spacing between atomic layers is 2.35 Å which corresponds to the (111) plane of Au.

Schematic diagrams and SEM images of each of the device architectures evaluated in this work are shown in Fig. 2. Fig. 2a shows a schematic representation of the control device structure without plasmonic particles and with a flat Au electrode. The structure consists of four layers deposited on an FTO coated glass substrate: an 80 nm-thick TiO_2 hole blocking layer, a 1 μm-thick TiO_2 mesoporous film, a 150 nm-thick PbS QDs film, and a 20 nm-thick Au electrode. An energy level diagram of the device is provided in Fig. 2e. Electrons are transferred from the conduction band of the PbS QDs to that of TiO_2, and then to the FTO, whereas holes in the PbS QDs move to the Au. A depletion region at the TiO_2–PbS interface promotes electron–hole pair separation and carrier injection. To investigate the effect of the plasmonic particles on the performance of the QD solar cells, plasmonic SGSs are added in two ways (Fig. 2b and c). The first method is to coat a monolayer of SGSs on top of the PbS film before the Au electrode is deposited (see Fig. 2b). This architecture is denoted as 'SGS on top'. The second method is to place the SGSs on the TiO_2 film first and then coat the PbS film on the SGS decorated TiO_2 film (Fig. 2c). This architecture is designated 'SGS inside'. In order to separately study the scattering effect of the nanodomes, bare silica spheres with the same average diameter of the SGSs were added into the device (see Fig. 2d). This control device is expected to provide the same scattering effect of the nanodomes without the LSPR effect. The cross-sectional SEM images of each device confirm the essential features of the schematic structure. Additional SEM images of the nanodome structures for the SGS-inside device (panel Fig. 2c) are shown in Fig. S2. Fig. 2f shows the distribution of SGSs on the substrate before the dip coating of PbS QDs. SGSs cover 20% of the surface area and the average distance between adjacent SGSs is about 400 nm.

The 'SGS on top' and 'SGS inside' structures (Fig. 2b and e) are expected to affect the incident light differently. For the 'SGSs on top' structure, light will couple with the SGSs after passing through the PbS film, and then will be scattered back into the film and/or excite LSPR modes that enhance light absorption near the PbS/SGS boundary. An advantage of this design is that it minimizes energy dissipation by the SGSs, because the photons strike the PbS film first. For the 'SGS inside' structure, the light interacts with the SGSs prior to propagating into the PbS layer. This morphology has two effects: the SGSs increase the absorption of nearby PbS QDs, and it causes nanodomes to form on the top Au contact which leads to additional light scattering. These two effects, enhancement of the PbS absorption by the LSPR modes and additional light scattering at the top contact, work in concert to enhance the overall efficiency. Though this latter geometry increases light absorption on the front side of the solar cell, the plasmonic enhancement and the nanodome scattering contributions act synergistically and more than compensate for the light loss.

The performance of the photovoltaic devices was tested under AM 1.5 conditions. The current–voltage (*J*–*V*) characteristics of four solar cells are shown in Fig. 3a, and the performance parameters of the solar cells are summarized in Table 1. Addition of the SGSs to the top of PbS film, 'SGS on top' structure, increases the short circuit current (J_{sc}) from 12.52 mA cm^{-2} to 15.10 mA cm^{-2}. When the SGSs are placed between the PbS film and the TiO_2 film, 'SGS inside' structure, a further enhancement was observed and the J_{sc} increases even more to 16.15 mA cm^{-2}, giving a 29% improvement over the control device. Thus, inclusion of SGSs improve device performance, however the 'SGS inside' architecture is superior – increasing the power conversion efficiency (PCE) from 3.09% without SGSs to 3.83% for the 'SGS-inside' device, by an enhancement of 24%.

To elucidate the physics underlying this enhancement, incident photon to current efficiency (IPCE) spectra and UV–vis absorption spectra of the solar cells were analyzed. Fig. 3b shows the IPCE spectra of the control device and the SGS devices. The device containing SiO_2 particles (no plasmonic activity) exhibits a slight increase in PCE (~2%) and the IPCE shows that this enhancement occurs in the wavelength range from 600 nm to 750 nm. This enhancement is attributed to an increase of light scattering by the nanodomes which form on the top Au electrode, and any associated LSPR activity arising from its nanostructure. Placement of SGSs on top of the PbS film ('SGS on top') causes a larger improvement in PCE (~7%). The IPCE is improved over the whole spectral range and the increase in the photon-to-electron

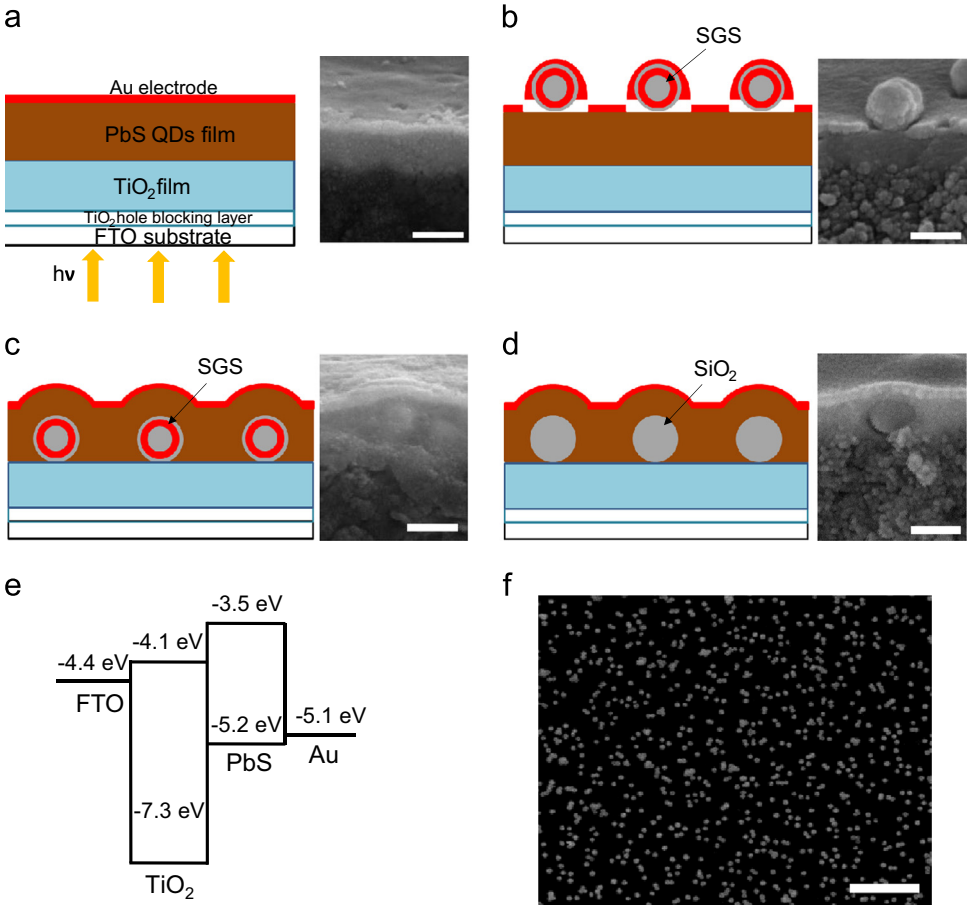

Fig. 2. Device architectures with cross-section view of the SEM images are shown here. Panel (a) is a control sample without SGSs. Panel (b) is a device with SGSs embedded between the PbS film and Au anode (called SGS on top). Panel (c) shows the case for SGSs submerged in the PbS film (called SGS inside). Panel (d) shows the case of SiO_2 spheres embedded in PbS film (SiO_2 inside). The scale bar in the SEM images is 200 nm. (e) An energy level diagram is shown for the standard device. Panel (f) shows an SEM image of a monolayer of SGSs prepared by drop coating and covering the surface area of a substrate by ~20%. Scale bar is 2 μm.

conversion in the red and near-IR regions is larger than for the cell with only nanodomes on the top electrode. This improvement indicates that the LSPR modes enhance the light absorption over a broad range and is consistent with FDTD simulations, vide infra. For the case where the SGSs are inserted between the PbS and TiO_2 films ('SGS inside') an even larger increase in PCE (~24%) is observed. The enhancement occurs over the whole spectral range, and it is the largest in the wavelength range of 600–750 nm.

Absorption spectra of the multilayer films are shown in Fig. 3c. The enhanced light absorption by the SGS containing films matches well with the improved photon-to-electron conversion in the IPCE spectra, and it indicates that the overlap of the absorption spectra of the PbS QDs and the SGSs LSPR modes, or light scattering by the SGSs, improves light absorption in the visible and near-IR regime. A slight redshift of the absorption peak in the PbS/SGS/TiO_2 structure may be caused by the high refractive index of the PbS matrix.

The 'SGS inside' device structure appears to improve the IPCE of the solar cells via multiple interacting effects. First, an increase in the photocurrent by SGSs arises from the coupling of LSPRs with incident light to generate a strong local electromagnetic field that facilitates light absorption by the PbS films [13]. This interaction decays strongly as a function of distance from the outer surface of the SGSs. Second, the 'SGS inside' structure causes the formation of nanodomes at the top Au electrode that produce enhanced scattering (Fig. 2d device) and an additional surface plasmon effect (Fig. 2b device) in the visible region. Therefore, in the 'SGS inside' device, the light intensity is increased through plasmonic interactions at both the top and bottom surfaces of PbS film, leading to higher light absorption in the near-IR regime [48]. These multiple effects increased the J_{sc} of the 'SGS inside' device by 29%, compared with the control device. Additional characterization of the solar cells by electrochemical impedance spectroscopy (EIS) analysis and open-circuit voltage decay (OCVD) techniques (see Fig. S3) supports this conclusion.

To further investigate the impact of the SGSs on the PbS-QD solar cells, numerical simulations of the optical field and the device absorbance spectra were performed using the finite-difference time-domain (FDTD) method. In particular, the PbS QD film structure (Fig. 2a) was simulated and then compared with the same structure for SGSs on top of the PbS QD film (Fig. 2b); geometric parameters were to mimic the actual device's structural features (see Fig. S2). Schematics of the simulated structures are shown in Fig. 4(a) where the light is incident from the bottom. Fig. 4a(i) shows a schematic diagram of the control device, which consists of a 150 nm thick PbS QD film on a 20 nm gold thin film back reflector. This structure was compared to the same active region with SGSs located in a 2D square lattice at the back side of the active region (Fig. 4a(ii)). The optical refractive indices for the PbS QD layer were obtained from experimental ellipsometry measurements (Supporting information, Fig. S4) and the optical constants for the SiO_2 and Au were taken from Palik [49]. The pitch of the SGSs in the simulation was $a=400$ nm, which corresponds to the approximate density of the SGSs as observed under SEM. The SGSs consisted of a silica core with a 90 nm diameter, a 20 nm gold intermediate layer, and a 7 nm outer silica shell. The position

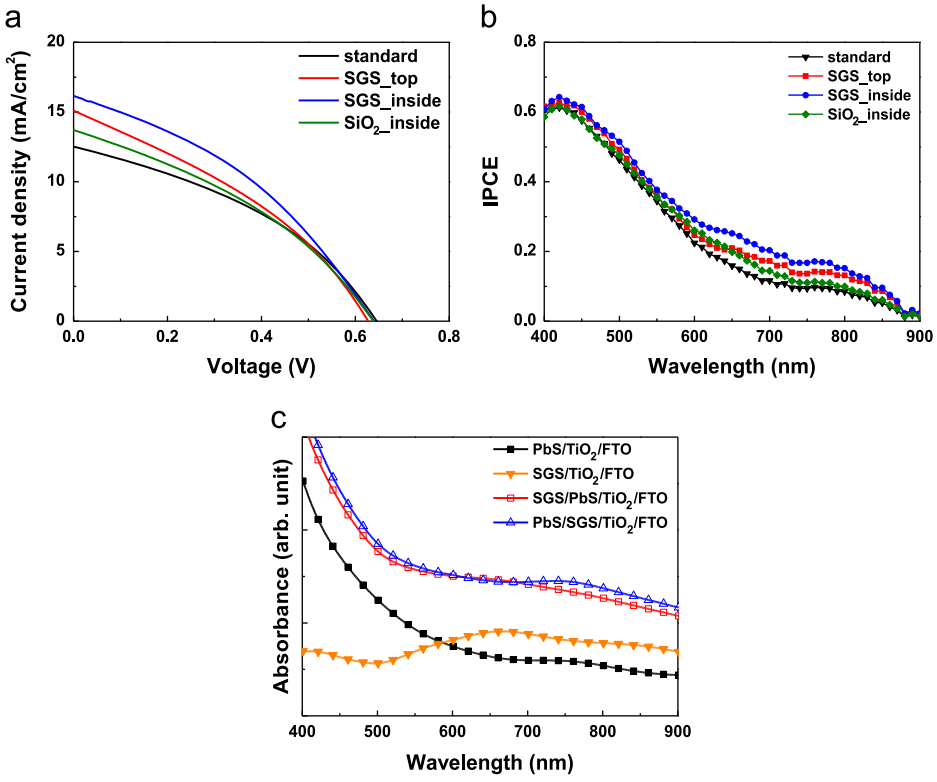

Fig. 3. *J–V* curves (a) and IPCE spectra (b) are shown for four device types: the standard sample without SGS, the SGS-on top device, the SGS-inside device, and the SiO_2 spheres inside. Panel (c) shows absorbance spectra of various tandem films: PbS/TiO_2/FTO, SGS/TiO_2/FTO, SGS/PbS/TiO_2/FTO, and PbS/SGS/TiO_2/FTO.

Table 1
Response of FTO/TiO_2/PbS/Au photovoltaic devices with and without SGSs under Simulated AM 1.5 (100 mW/cm^2).

Device description	J_{sc} (mA/cm^2)	V_{oc} (V)	FF (%)	η (%)
FTO/TiO_2/PbS/Au (standard)	12.52	0.65	38.16	3.09
FTO/TiO_2/PbS/SGS/Au (SGS on top)	15.10	0.63	34.83	3.30
FTO/TiO_2/SGS/PbS/Au (SGS inside)	16.15	0.64	37.04	3.83
FTO/TiO_2/SiO_2/PbS/Au (SiO_2 inside)	13.71	0.64	35.90	3.15

dependent absorption per unit volume was calculated from the divergence of the Poynting vector $\vec{P}$:

$$A(r,\lambda) = \frac{1}{2} real\left\{\vec{\nabla} \cdot \vec{P}\right\} = \tfrac{1}{2}\epsilon_i(\lambda)\omega|\mathbf{E}(\boldsymbol{r},\lambda)|^2 \quad (1)$$

where $\varepsilon_i(\lambda)$ is the imaginary part of the permittivity, $\omega = 2\pi c/\lambda$ is the photon angular frequency, c is the speed of light, and $\mathbf{E}(\boldsymbol{r}, \lambda)$ is the position and wavelength-dependent electric field vector. This treatment eliminated any parasitic absorption that may occur in the SGSs.

Results of the calculations indicate that the addition of the plasmonic SGSs enhances the absorption for wavelengths longer than 520 nm. Fig. 4(b) shows the local absorption per unit volume (in units of nm^{-3}) for the two structures shown in Fig. 4(a) at $\lambda = 680$ nm where a significant increase in IPCE was experimentally observed (Fig. 3b) after adding SGSs. The incident light proceeds from the PbS QD layer toward the Au layer and the electric field vector of the light is parallel to the *x*-axis in the simulation. Dashed white lines indicate the location of the 150 nm thick PbS QD layer and the 20 nm thick Au reflector, as well as the outline of the SGSs. About a 64% enhancement in absorption occurs through the photoactive region at this wavelength ($\lambda = 680$ nm); when the localized surface plasmon resonance of the SGS is excited, it scatters light back toward the PbS layer. A relatively strong increase in the absorption near the bottom of the PbS layer is caused by the superposition of light that SGSs scatter at high angles. This result supports the experimental observation that the SGSs at the top of the PbS film increase the IPCE in the red and near-IR regions by up to 50% compared with that of the control sample.

The images in Fig. 5 summarize the FDTD simulation and they display the dual effects arising from the 'SGS inside' architecture . First, the absorbance of the PbS QD film embedded with SGSs at the TiO_2/PbS interface was calculated on the assumption that the Au reflector film was flat. As shown in Fig. 5(a), the embedded SGSs strongly enhance the absorption of light ($\lambda = 680$ nm) in the PbS QD layer because of localized surface plasmons. A quantitative comparison indicates that the embedded SGS ('SGS inside' structure) leads to more light absorption than placing the SGS on the backside of Au film ('SGS on top'); see Figs. 5a and 4b. This finding is consistent with the experimental results in Fig. 3. To understand the role of the nanodome separately, the influence of introducing a curved PbS QD layer surface on the local electric field intensity concentration and the light absorption by the PbS QD film was investigated. The radius of curvature of the spherical dome was chosen to be ~230 nm and its extent above the height is ~40 nm. Fig. 5(b) plots the local absorption per unit volume in the PbS QD layer and it shows that the uneven surface causes an additional increase in the local electric field intensity. These two effects are combined for the architecture simulated in Fig. 5C, and it reveals an enhanced absorbance over that found in Fig. 5A and B. Mie efficiencies for the scattering and absorption of light by an isolated SGS in air are also presented in Fig. S5. Resonance peaks are found near the wavelengths where the energy conversion efficiency of PbS solar cells is increased by SGS particles. These simulation results support the conclusion that the 'SGS inside' architecture has a dual effect that improves the performance of PbS solar cells.

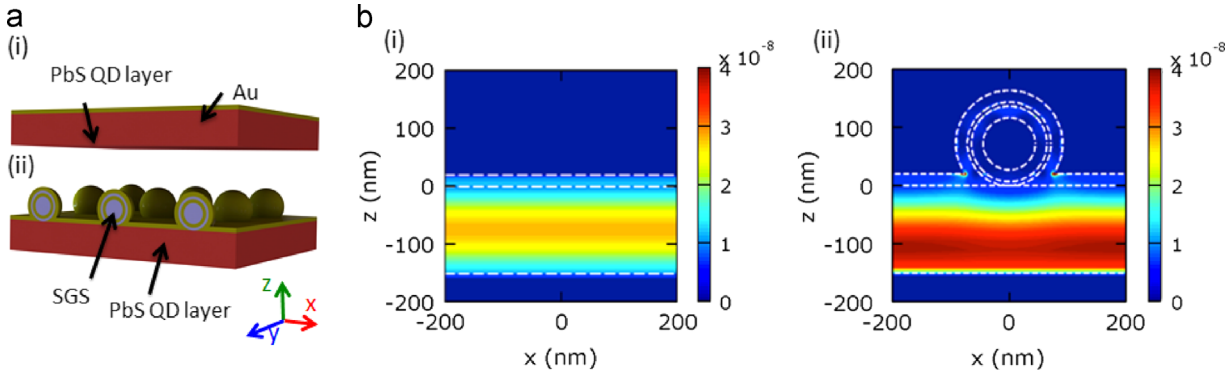

Fig. 4. Panel (a) shows schematic diagrams of the (i) 150 nm PbS QD thin film on 20 nm Au back reflector and (ii) same structure with SGSs on the top of PbS QD film. Panel (b) shows a spatial distribution of the light absorption per unit volume (in units of nm^{-3}) at $\lambda=680$ nm for the two structures (the incident light is from the bottom and hits the PbS QD layer first).

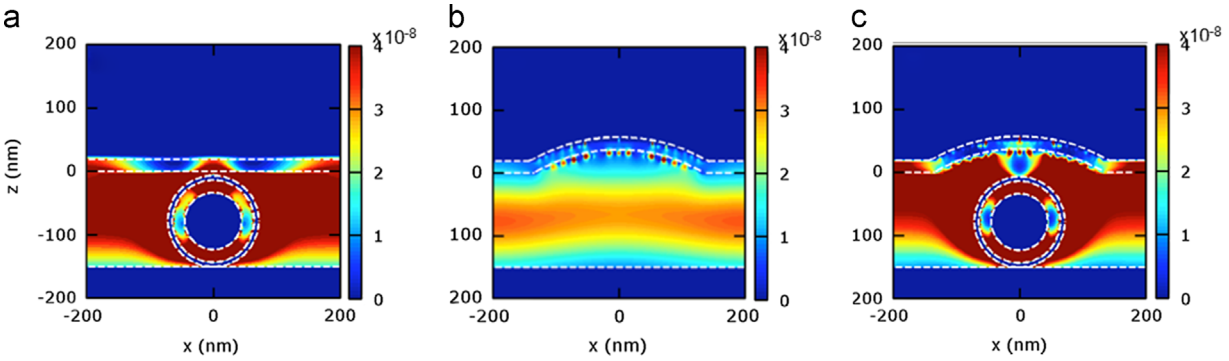

Fig. 5. Absorption per unit volume at $\lambda=680$ nm is shown for (a) PbS QD thin film with embedded SGS and smooth Au surface, (b) PbS QD thin film with the curved Au surface, and (c) PbS QD thin film with SGS and the curved Au surface.

4. Conclusion

Plasmonic SGSs were prepared and incorporated into PbS QD thin film solar cells to improve the light harvesting. The SGSs can improve light absorption over the visible (600–750 nm) and near IR regime (800–1000 nm) where PbS QDs with the bandgap of ~1.67 eV absorb photons weakly. Experimental and theoretical studies show that the SGSs enhance light absorption in the PbS layer by the excitation of LSPRs. In addition, SGSs cause additional light scattering by creating the curved nanodome structure at the Au/PbS interface. These observations indicate a synergistic effect of LSPRs and light scattering on enhanced light absorption can be realized by placing the SGSs at the PbS–TiO_2 interface. These effects increase the energy conversion efficiency of PbS thin film solar cells by 24%. This strategy is general and can be applied to improving the performance of other thin film solar cells.

Acknowledgments

This work was supported by the National Science Foundation (Grant nos. DMR-0847319 and CBET-1235979 to J.K. Lee) and (Grant no. CMMI-1233151 to P.W. Leu), and by a grant from the US Department of Energy (Grant no. ER46430) to DHW.

Appendix A. Supporting information

Supplementary data associated with this article can be found in the online version at http://dx.doi.org/10.1016/j.solmat.2014.06.001.

References

[1] D.V. Talapin, J.S. Lee, M.V. Kovalenko, E.V. Shevchenko, Chem. Rev. 110 (2010) 389–458.
[2] J.A. Tang, E.H. Sargent, Adv. Mater. 23 (2011) 12–29.
[3] R.J. Ellingson, M.C. Beard, J.C. Johnson, P.R. Yu, O.I. Micic, A.J. Nozik, A. Shabaev, A.L. Efros, Nano Lett. 5 (2005) 865–871.
[4] S.A. McDonald, G. Konstantatos, S.G. Zhang, P.W. Cyr, E.J.D. Klem, L. Levina, E.H. Sargent, Nat. Mater. 4 (2005) 138–142.
[5] J.M. Luther, M. Law, M.C. Beard, Q. Song, M.O. Reese, R.J. Ellingson, A.J. Nozik, Nano Lett. 8 (2008) 3488–3492.
[6] W.L. Ma, S.L. Swisher, T. Ewers, J. Engel, V.E. Ferry, H.A. Atwater, A.P. Alivisatos, ACS Nano 5 (2011) 8140–8147.
[7] J.B. Gao, C.L. Perkins, J.M. Luther, M.C. Hanna, H.Y. Chen, O.E. Semonin, A.J. Nozik, R.J. Ellingson, M.C. Beard, Nano Lett. 11 (2011) 3263–3266.
[8] O.E. Semonin, J.M. Luther, S. Choi, H.Y. Chen, J.B. Gao, A.J. Nozik, M.C. Beard, Science 334 (2011) 1530–1533.
[9] A.G. Pattantyus-Abraham, I.J. Kramer, A.R. Barkhouse, X.H. Wang, G. Konstantatos, R. Debnath, L. Levina, I. Raabe, M.K. Nazeeruddin, M. Gratzel, E.H. Sargent, ACS Nano 4 (2010) 3374–3380.
[10] J.-W. Lee, D.-Y. Son, T.K. Ahn, H.-W. Shin, I.-Y. Kim, S.-J. Hwang, M.J. Ko, S. Sul, H. Han, N.-G. Park, Sci. Rep. 3 (1050) (2013) 1–8.
[11] D.A.R. Barkhouse, A.G. Pattantyus-Abraham, L. Levina, E.H. Sargent, ACS Nano 2 (2008) 2356–2362.
[12] K.W. Johnston, A.G. Pattantyus-Abraham, J.P. Clifford, S.H. Myrskog, S. Hoogland, H. Shukla, J.D. Klem, L. Levina, E.H. Sargent, Appl. Phys. Lett. 92 (2008) 122111.
[13] H.A. Atwater, A. Polman, Nat. Mater. 9 (2010) 205–213.
[14] V.E. Ferry, M.A. Verschuuren, H.B.T. Li, E. Verhagen, R.J. Walters, R.E.I. Schropp, H.A. Atwater, A. Polman, Opt. Express 18 (2010) A237–A245.
[15] P. Spinelli, V.E. Ferry, J. van de Groep, M. van Lare, M.A. Verschuuren, R.E.I. Schropp, H.A. Atwater, A. Polman, J. Opt. 14 (2012) 024002.
[16] M.G. Deceglie, V.E. Ferry, A.P. Alivisatos, H.A. Atwater, Nano Lett. 12 (2012) 2894–2900.
[17] I.K. Ding, J. Zhu, W.S. Cai, S.J. Moon, N. Cai, P. Wang, S.M. Zakeeruddin, M. Gratzel, M.L. Brongersma, Y. Cui, M.D. McGehee, Adv. Energy Mater. 1 (2011) 52–57.
[18] J.F. Qi, X.N. Dang, P.T. Hammond, A.M. Belcher, ACS Nano 5 (2011) 7108–7116.
[19] X.H. Li, W.C.H. Choy, L.J. Huo, F.X. Xie, W.E.I. Sha, B.F. Ding, X. Guo, Y.F. Li, J.H. Hou, J.B. You, Y. Yang, Adv. Mater. 24 (2012) 3046–3052.

[20] D.H. Wang, D.Y. Kim, K.W. Choi, J.H. Seo, S.H. Im, J.H. Park, O.O. Park, A.J. Heeger, Angew. Chem. Int. Ed. 50 (2011) 5519–5523.
[21] A.P. Kulkarni, K.M. Noone, K. Munechika, S.R. Guyer, D.S. Ginger, Nano Lett. 10 (2010) 1501–1505.
[22] S.J. Oldenburg, R.D. Averitt, S.L. Westcott, N.J. Halas, Chem. Phys. Lett. 288 (1998) 243–247.
[23] C. Loo, A. Lin, L. Hirsch, M.H. Lee, J. Barton, N.J. Halas, J. West, R. Drezek, Technol. Cancer Res. Treat. 3 (2004) 33–40.
[24] A.M. Schwartzberg, T.Y. Olson, C.E. Talley, J.Z. Zhang, J. Phys. Chem. B 110 (2006) 19935–19944.
[25] J.Y. Chen, J.M. McLellan, A. Siekkinen, Y.J. Xiong, Z.Y. Li, Y.N. Xia, J. Am. Chem. Soc. 128 (2006) 14776–14777.
[26] S.E. Skrabalak, J.Y. Chen, Y.G. Sun, X.M. Lu, L. Au, C.M. Cobley, Y.N. Xia, Acc. Chem. Res. 41 (2008) 1587–1595.
[27] H. Wang, Y.P. Wu, B. Lassiter, C.L. Nehl, J.H. Hafner, P. Nordlander, N.J. Halas, Proc. Natl. Acad. Sci. USA 103 (2006) 10856–10860.
[28] J.B. Lassiter, M.W. Knight, N.A. Mirin, N.J. Halas, Nano Lett. 9 (2009) 4326–4332.
[29] Y. Lu, G.L. Liu, J. Kim, Y.X. Mejia, L.P. Lee, Nano Lett. 5 (2005) 119–124.
[30] T.K. Sau, C.J. Murphy, Langmuir 20 (2004) 6414–6420.
[31] E.C. Dreaden, A.M. Alkilany, X.H. Huang, C.J. Murphy, M.A. El-Sayed, Chem. Soc. Rev. 41 (2012) 2740–2779.
[32] X.H. Huang, I.H. El-Sayed, W. Qian, M.A. El-Sayed, J. Am. Chem. Soc. 128 (2006) 2115–2120.
[33] X.N. Dang, J.F. Qi, M.T. Klug, P.Y. Chen, D.S. Yun, N.X. Fang, P.T. Hammond, A.M. Belcher, Nano Lett. 13 (2013) 637–642.
[34] S. Chang, Q. Li, X.D. Xiao, K.Y. Wong, T. Chen, Energy Environ. Sci. 5 (2012) 9444–9448.
[35] B. Ding, B.J. Lee, M.J. Yang, H.S. Jung, J.K. Lee, Adv. Energy Mater. 1 (2011) 415–421.
[36] B. Ding, M.J. Yang, B.J. Lee, J.K. Lee, RSC Adv. 3 (2013) 9690–9697.
[37] D. Paz-Soldan, A. Lee, S.M. Thon, M.M. Adachi, H. Dong, P. Maraghechi, M. Yuan, A.J. Labelle, S. Hoogland, K. Liu, E. Kumacheva, E.H. Sargent, Nano Lett. 13 (2013) 1502–1508.
[38] E. Prodan, C. Radloff, N.J. Halas, P. Nordlander, Science 302 (2003) 419–422.
[39] J.M. Luther, M. Law, Q. Song, C.L. Perkins, M.C. Beard, A.J. Nozik, ACS Nano 2 (2008) 271–280.
[40] O. Peña-Rodríguez, U. Pal, J. Phys. Chem. C 114 (2010) 4414–4417.
[41] O. Peña-Rodríguez, A. Rivera, M. Campoy-Quiles, U. Pal, Nanoscale 5 (2013) 209–216.
[42] O. Peña-Rodríguez, U. Pal, Nanoscale 3 (2011) 3609–3612.
[43] O. Peña-Rodríguez, U. Pal, Nanoscale Res. Lett. 6 (279) (2011) 1–5.
[44] H. Wang, D.W. Brandl, F. Le, P. Nordlander, N.J. Halas, Nano Lett. 6 (2006) 827–832.
[45] C. Graf, A. van Blaaderen, Langmuir 18 (2002) 524–534.
[46] C. Graf, D.L.J. Vossen, A. Imhof, A. van Blaaderen, Langmuir 19 (2003) 6693–6700.
[47] J.F. Li, Y.F. Huang, Y. Ding, Z.L. Yang, S.B. Li, X.S. Zhou, F.R. Fan, W. Zhang, Z.Y. Zhou, D.Y. Wu, B. Ren, Z.L. Wang, Z.Q. Tian, Nature 464 (2010) 392–395.
[48] V.E. Ferry, L.A. Sweatlock, D. Pacifici, H.A. Atwater, Nano Lett. 8 (2008) 4391–4397.
[49] E.D. Palik, Handbook of Optical Constants of Solids, Academic Press, San Diego, 1997.
[50] B.E. Brinson, J.B. Lassiter, C.S. Levin, R. Bardhan, N. Mirin, N.J. Halas, Langmuir 24 (2008) 14166–14171.
[51] W. Stober, A. Fink, E. Bohn, J. Colloid Interface Sci. 26 (1968) 62–69.
[52] D.G. Duff, A. Baiker, P.P. Edwards, Langmuir 9 (1993) 2301–2309.
[53] M.A. Hines, G.D. Scholes, Adv. Mater. 15 (2003) 1844–1849.
[54] A. Zaban, M. Greenshtein, J. Bisquert, ChemPhysChem 4 (2003) 859–864.